CHEMISTRY OF MATERIALS
Article

Chem. Mater. **2010,** *22,* 3241–3250 3241
DOI:10.1021/cm100476m

Polar Hexagonal Tungsten Oxide (HTO) Materials: (1) Synthesis, Characterization, Functional Properties, and Structure−Property Relationships in $A_2(MoO_3)_3(SeO_3)$ ($A = Rb^+$ and Tl^+) and (2) Classification, Structural Distortions, and Second-Harmonic Generating Properties of Known Polar HTOs

Hong Young Chang, Sun Woo Kim, and P. Shiv Halasyamani*

Department of Chemistry, University of Houston, 136 Fleming Building, Houston, Texas 77204-5003

Received February 15, 2010. Revised Manuscript Received April 7, 2010

Two new polar noncentrosymmetric (NCS) oxides, $Rb_2(MoO_3)_3(SeO_3)$ and $Tl_2(MoO_3)_3(SeO_3)$, have been synthesized and characterized. The materials exhibit the layered hexagonal tungsten oxide (HTO) structural topology—Class 2, i.e., the MoO_6 layers are "capped" on one side by the SeO_3 polyhedra. The Rb^+ and Tl^+ cations are found between the layers. The Mo^{6+} and Se^{4+} cations are present in asymmetric coordination environments that are attributable to second-order Jahn−Teller (SOJT) effects. In addition to structural characterization, the materials were characterized by second-harmonic generation (SHG), piezoelectric, and polarization measurements. SHG measurements using 1064-nm radiation revealed doubling efficiencies of 300 and 400 × α-SiO_2 for the Rb- and Tl-phases, respectively. Piezoelectric experiments revealed d_{33} values of ∼9−13 pm/V. Polarization measurements indicate that the materials are not ferroelectric, i.e., the polarization is not "switchable". The materials are pyroelectric, with total pyroelectric coefficients (p), at 45 °C, of $-1.1\ \mu C\ m^{-2}\ K^{-1}$ for $Rb_2(MoO_3)_3(SeO_3)$ and $-2.1\ \mu C\ m^{-2}\ K^{-1}$ for $Tl_2(MoO_3)_3(SeO_3)$. Thermogravimetry, differential scanning calorimetry, UV−vis, and infrared spectroscopy measurements were also performed. We also examine all of the known polar HTO-type materials to gain a better understanding of the functional properties and structure−property relationships. Crystal data for $Rb_2(MoO_3)_3(SeO_3)$: hexagonal, space group $P6_3$ (No. 173), $a = b = 7.2992(14)$ Å, $c = 11.978(5)$ Å, $V = 552.7(3)$ Å^3, and $Z = 2$; crystal data for $Tl_2(MoO_3)_3(SeO_3)$: trigonal, space group $P31c$ (No. 159), $a = b = 7.2867(10)$ Å, $c = 11.794(3)$ Å, $V = 542.33(18)$ Å^3, and $Z = 2$.

Introduction

The hexagonal tungsten bronze (HTB) family of materials represents a diverse and fascinating group of compounds. Described and synthesized by Magneli and others,[1−6] the structural archetype may be formulated as A_xWO_3, where A is an alkali metal and $x \approx 0.3$. The structure consists of corner-shared WO_6 octahedra that form a hexagonal network wherein the A cation resides (see Figure 1). HTB compounds are of interest not only for their structural diversity, because a variety of cations may substitute for W^{6+} as well as the A cation,[2,7] but also for their functional properties.[8−16] Many HTBs are macroscopically polar, indicating that important functional properties such as second-harmonic generation, piezoelectricity, ferroelectricity, and pyroelectricity are possible. This macroscopic polarity originates in the WO_6, or other d^0 centered oxide octahedra, i.e., NbO_6, MoO_6, etc.[17,18] In these oxide octahedra, the d^0 cation is often displaced toward one or more of the oxide ligands, which results in a local dipole moment. The local polarity "constructively adds" and results in a macroscopically polar material.

*Author to whom correspondence should be addressed. E-mail: psh@uh.edu.

(1) Magneli, A. *Acta Chem. Scand.* **1951**, *5*, 670.
(2) Magneli, A. *Acta Chem. Scand.* **1953**, *7*, 315.
(3) Goodman, P. *Acta Crystallogr., Sect. B: Struct. Crystallogr. Cryst. Chem.* **1976**, *B32*, 3280.
(4) Galasso, F.; Darby, W. *J. Phys. Chem.* **1964**, *68*, 1253.
(5) Hussain, A.; Kihlborg, L.; Klug, A. *J. Solid State Chem.* **1978**, *25*, 189.
(6) Kudo, T.; Oi, J.; Kishimoto, A.; Inoue, H. *Solid State Ionics* **1990**, *40*/*41*, 567.
(7) Lee, K.-S.; D.-K., S.; Whangbo, M.-H. *J. Am. Chem. Soc.* **1997**, *119*, 4043.
(8) Yanovskii, V. K.; Voronkova, V. I.; Klimova, I. P. *Ferroelectrics* **1983**, *48*, 239.
(9) Yanovskii, V. K.; Voronkova, V. I.; Petrovskaya, T. P. *Izv. Akad. Nauk SSSR, Neorg. Mater.* **1983**, *19*, 1910.
(10) Isupov, V. A. *Ferroelectrics* **1985**, *65*, 181.
(11) Tsuyumoto, I.; Kishimoto, A.; Kudo, T. *Solid State Ionics* **1993**, *59*, 211.
(12) Klimova, I. P.; Voronkova, V. I.; Yanovskii, V. K. *Izv. Akad. Nauk SSSR, Neorg. Mater.* **1995**, *31*, 245.
(13) Tsuyumoto, I.; Kudo, T. *Sens. Actuators, B* **1996**, *B30*, 95.
(14) Tsuyumoto, I.; Kudo, T. *Mater. Res. Bull.* **1996**, *31*, 17.
(15) Isupov, V. A. *Ferroelectrics* **1998**, *211*, 209.
(16) Chang, H. Y.; Sivakumar, T.; Ok, K. M.; Halasyamani, P. S. *Inorg. Chem.* **2008**, *47*, 8511.
(17) Isupov, V. A.; Agranovskaya, A. I.; Bryzhina, M. F. *Kristallografiya* **1963**, *8*, 108.
(18) Yanovskii, V. K.; Voronkova, V. I.; Klimova, I. P. *Ferroelectrics* **1983**, *48*, 239.

Published on Web 04/27/2010

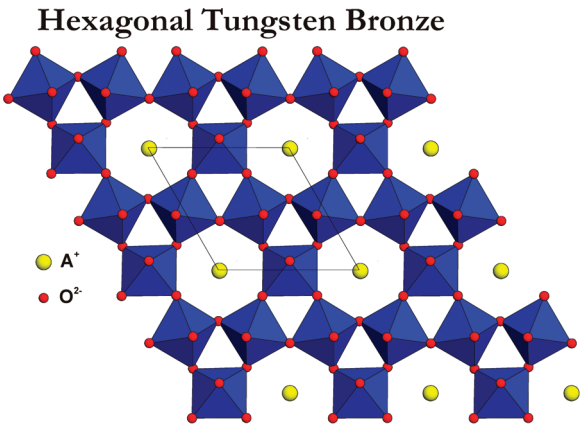

Figure 1. Polyhedral diagram of the archetypal hexagonal tungsten bronze (HTB) structure. The yellow spheres represent alkali metals, and the red spheres are oxide anions.

Related to the HTB structure is the hexagonal tungsten oxide (HTO) topology. The oxide layers in HTBs and HTOs are very similar; however, compounds that exhibit the HTO-type structures have a tendency to be layered, as opposed to being three-dimensional with the HTBs. For the polar HTOs, one observes "capping" of the layers on one or both sides by selenite $(SeO_3)^{2-}$ or tellurite $(TeO_3)^{2-}$, as well as methyl phosphonate $(O_3PCH_3)^{2-}$ groups (see Figure 2). Even with this capping on both sides, macroscopic polarity is often retained.

One of the objectives of this paper is to not only report on the synthesis, characterization, and functional properties of two new HTO-type materials, $Rb_2(MoO_3)_3(SeO_3)$ and $Tl_2(MoO_3)_3(SeO_3)$, but also to examine HTOs as a whole, to better understand their structure−property relationships. We are able to divide the polar HTO-type oxides into two groups: Class 1 ("capped" on both sides) and Class 2 ("capped" on one side) (see Figures 2a and 2b). Class 1 materials include $A(V^{5+}O_2)_3(SeO_3)_2$ ($A = NH_4^+$, K^+, Rb^+, Cs^+, or Tl^+),[19−22] $Cs(V^{5+}O_2)_3(TeO_3)_2$,[23] and $A(V^{5+}O_2)_3(PO_3CH_3)_2$ ($A = NH_4^+$ or K^+).[24] For materials in Class 1, the VO_6 octahedral layers are "capped" on both sides by a lone pair or a methyl phosphonate group (see Figure 2a). Class 2 materials include $A_2(Mo^{6+}O_3)_3(SeO_3)$ ($A = NH_4^+$ or Cs^+),[25] $A_2(Mo^{6+}O_3)_3(TeO_3)$ ($A = NH_4^+$ or Cs^+),[26] $A_2(W^{6+}O_3)_3(SeO_3)$ ($A = NH_4^+$ or Cs^+),[27] $Rb_2(W^{6+}O_3)_3(TeO_3)$,[28] $A_2(Mo^{6+}O_3)_3(PO_3CH_3)$ ($A = Rb^+$, Cs^+, or Tl^+),[29,30] and $Cs_2(W^{6+}O_3)_3(PO_3CH_3)$.[31] With these materials, the octahedral layers are "capped" on one side by a lone pair or a methyl phosphonate group (see Figure 2b). In this paper, we report on the synthesis and characterization of two new polar Class 2 HTO-type materials: $Rb_2(MoO_3)_3(SeO_3)$ and $Tl_2(MoO_3)_3(SeO_3)$. With the reported materials, in addition to the crystal structure, we also performed second-harmonic generation (SHG), piezoelectricity, polarization, thermogravimetry, differential scanning calorimetry, infrared, and UV−visible measurements. We also examine the reported polar HTOs as a whole, to gain a better understanding of the bonding interactions that result in different metal−oxygen bond asymmetries. We also discuss structure−property relationships, i.e., the relationship between the structural distortions and functional properties for all the reported polar HTO materials.

Experimental Section

Reagents. Rb_2CO_3 (Alfa Aesar, 99%), Cs_2CO_3 (Alfa Aesar, 99%), Tl_2CO_3 (Alfa Aesar, 99%), SeO_2 (Alfa Aesar, 99%), and MoO_3 (Aldrich, 99%) were used as received. $Rb_2Mo_3O_{10}$, $Cs_2Mo_3O_{10}$, and Tl_2MoO_4, were synthesized as described.[32−35]

Synthesis. Crystals of $Rb_2(MoO_3)_3(SeO_3)$ were grown by combining 0.762 g (3.30×10^{-3} mol) of Rb_2CO_3, 0.366 g (3.30×10^{-3} mol) of SeO_2, and 1.260 g (8.75×10^{-3} mol) of MoO_3 with 5 mL of H_2O. Crystals of $Tl_2(MoO_3)_3(SeO_3)$ were grown by combining 0.510 g (1.09×10^{-3} mol) of Tl_2CO_3, 0.151 g (1.36×10^{-3} mol) of SeO_2, and 0.384 g (2.67×10^{-3} mol) of MoO_3 with 5 mL of H_2O. The respective solutions were placed in 23-mL Teflon-lined autoclaves that were subsequently sealed. The autoclaves were gradually heated to 230 °C, held for 3 d, and cooled slowly to room temperature at a rate of 6 °C/h. The mother liquor was decanted from the products, and the products were recovered by filtration and washed with distilled water. Colorless hexagonal rod-shaped crystals and colorless rod-shaped crystals of $Rb_2(MoO_3)_3(SeO_3)$ and $Tl_2(MoO_3)_3(SeO_3)$, respectively, were recovered. The yields were 50% for $Rb_2(MoO_3)_3(SeO_3)$ and 80% for $Tl_2(MoO_3)_3(SeO_3)$, on the basis of MoO_3.

Bulk samples of $Rb_2(MoO_3)_3(SeO_3)$ and $Tl_2(MoO_3)_3(SeO_3)$ were prepared by standard solid-state techniques. A stoichiometric mixture of $Rb_2Mo_3O_{10}$ (0.500 g, 0.81×10^{-3} mol) and SeO_2 (0.090 g, 0.81×10^{-3} mol) for $Rb_2(MoO_3)_3(SeO_3)$, and a stoichiometric mixture of Tl_2MoO_4 (0.500 g, 0.88×10^{-3} mol), MoO_3 (0.253 g, 1.76×10^{-3} mol), and SeO_2 (0.096 g, 0.88×10^{-3} mol) for $Tl_2(MoO_3)_3(SeO_3)$, were ground with an agate mortar and pestle and introduced into separate fused-silica tubes that were subsequently evacuated under vacuum and sealed. The tubes were heated to 400 and 330 °C, respectively, for 24 h and cooled slowly to room temperature at a rate of 10 °C/h. $Cs_2(MoO_3)_3(SeO_3)$ was also synthesized by standard solid-state techniques by combining a stoichiometric mixture of

(19) Vaughey, J. T.; Harrison, W. T. A.; Dussack, L. L.; Jacobson, A. J. *Inorg. Chem.* **1994**, *33*, 4370.
(20) Harrison, W. T. A.; Dussack, L. L.; Jacobson, A. J. *Acta Crystallogr., Sect. C: Cryst. Struct. Commun.* **1995**, *C51*, 2473.
(21) Harrison, W. T. A. *Acta Crystallogr., Sect. C: Cryst. Struct. Commun.* **2000**, *C56*, 422.
(22) Chang, H. Y.; Kim, S. H.; Ok, K. M.; Halasyamani, P. S. *Chem. Mater.* **2009**, *21*, 1654.
(23) Harrison, W. T. A.; Buttery, J. H. N. *Z. Anorg. Allg. Chem.* **2000**, *626*, 867.
(24) Harrison, W. T. A.; Dussack, L. L.; Jacobson, A. J. *Inorg. Chem.* **1996**, *35*, 1461.
(25) Harrison, W. T. A.; Dussack, L. L.; Jacobson, A. J. *Inorg. Chem.* **1994**, *33*, 6043.
(26) Balraj, V.; Vidyasagar, K. *Inorg. Chem.* **1998**, *37*, 4764.
(27) Harrison, W. T. A.; Dussack, L. L.; Vogt, T.; Jacobson, A. J. *J. Solid State Chem.* **1995**, *120*, 112.
(28) Goodey, J.; Ok, K. M.; Broussard, J.; Hofmann, C.; Escobedo, F. V.; Halasyamani, P. S. *J. Solid State Chem.* **2003**, *175*, 3.
(29) Harrison, W. T. A.; Dussack, L. L.; Jacobson, A. J. *Inorg. Chem.* **1995**, *34*, 4774.
(30) Harrison, W. T. A.; Dussack, L. L.; Jacobson, A. J. *J. Solid State Chem.* **1998**, *138*, 365.
(31) Harrison, W. T.; Dussack, L. L.; Vaughey, J. T.; Vogt, T.; Jacobson, A. J. *J. Mater. Chem.* **1996**, *6*, 81.
(32) Kools, F. X. N. M.; Koster, A. S.; Rieck, G. D. *Acta Crystallogr., Sect. B: Struct. Crystallogr. Cryst. Chem.* **1970**, *B26*, 1974.
(33) Sleight, A. W.; Bierlein, J. D.; Bierstedt, P. E. *J. Chem. Phys.* **1975**, *62*, 2826.
(34) Okada, K.; Ossaka, J. *Acta Crystallogr., Sect. B: Struct. Crystallogr. Cryst. Chem.* **1979**, *B35*, 2189.
(35) Friese, K.; Madariaga, G.; Breczewski, T. *Acta Crystallogr., Sect. C: Cryst. Struct. Commun.* **1999**, *C55*, 1753.

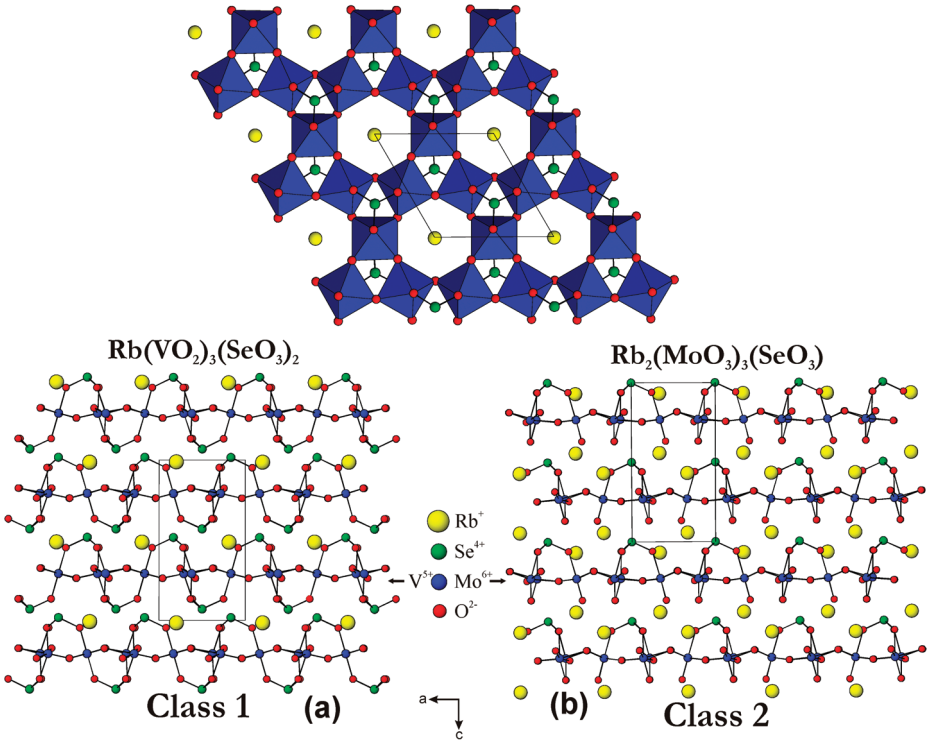

Figure 2. (top) Polyhedral diagram of the hexagonal tungsten oxide (HTO) topology: (a) ball-and-stick diagram of a Class 1 HTO−$Rb(VO_2)_3(SeO_3)_2$ and (b) ball-and-stick diagram of a Class 2 HTO−$Rb_2(MoO_3)_3(SeO_3)$. Note that, with the Class 1 HTO, the lone-pair polyhedra are directed "up" and "down", whereas for the Class 2 HTO, the lone-pair polyhedra are only directed "up".

$Cs_2Mo_3O_{12}$ (0.500 g, 0.70×10^{-3} mol) and SeO_2 (0.078 g, 0.70×10^{-3} mol) in a fused-silica tube that was evacuated, sealed, and heated to 400 °C.

Single-Crystal X-ray Diffraction. For $Rb_2(MoO_3)_3(SeO_3)$ and $Tl_2(MoO_3)_3(SeO_3)$, colorless hexagonal rod-shaped (0.06 mm × 0.02 mm × 0.02 mm) and colorless rod-shaped (0.08 mm × 0.04 mm × 0.04 mm) crystals were used for single-crystal data collection, respectively. Data were collected using a Siemens SMART APEX diffractometer equipped with a 1K CCD area detector, using graphite-monochromated Mo Kα radiation. A hemisphere of data was collected using a narrow-frame method with scan widths of 0.50° in ω, and an exposure time of 40 s per frame. The first 50 frames were measured again at the end of the data collection to monitor instrument and crystal stability. The data were integrated using the Siemens SAINT program,[36] with the intensities corrected for Lorentz polarization, air absorption, and absorption attributable to the variation in the path length through the detector face plate. Psi-scans were used for the absorption correction on the data. The data were solved and refined using SHELXS-97 and SHELXL-97, respectively.[37−39] All of the atoms were refined with anisotropic thermal parameters, and the refinement converged for $I > 2\sigma(I)$. All calculations were performed using the WinGX-98 crystallographic software package.[40] A symmetry analysis on the $Tl_2(MoO_3)_3(SeO_3)$ structure using PLATON[41] revealed considerable pseudo-symmetry that was consistent with small atomic shifts of the Mo, Se, and O atoms from possible positions in space group $P6_3mc$. However, the reflection intensity conditions required for a *hexagonal system* are strongly violated in the data collected for the $Tl_2(MoO_3)_3(SeO_3)$ structure. Specifically, the condition $\{(h,k,l) = (-k, h+k, l) = (-h-k, h, l) = (-h, -k, l) = (k, -h-k, l) = (h+k, -h, l)\}$, which is required to satisfy the existence of 6-fold axis symmetry, is severely violated. Instead, the conditions $\{(h,k,l) = (-h-k, h, l) = (k, -h-k, l)\}$ and $\{(-k, h+k, l) = (-h, -k, l) = (h+k, -h, l)\}$ are satisfied to reflect 3-fold axis symmetry. Thus, the data for $Tl_2(MoO_3)_3(SeO_3)$ are consistent for a *trigonal system*. Crystallographic data, atomic coordinates, and selected bond distances for $Rb_2(MoO_3)_3(SeO_3)$ and $Tl_2(MoO_3)_3(SeO_3)$ are given in Tables 1, 2, and 3, respectively, with additional details given in the Supporting Information.

Powder X-ray Diffraction. Powder X-ray diffraction (XRD) data were collected using a PANalytical X'Pert PRO diffractometer, using Cu Kα radiation. The 2θ range was 10°−60°, with a step size of 0.008° and a fixed time of 0.3 s. The experimental powder XRD data are in good agreement with the calculated data, based on the single-crystal models. In addition, the powder XRD patterns for $Cs_2(MoO_3)_3(SeO_3)$ are in good agreement with the reported data (see Figures S1 and S2 in the Supporting Information).[25]

Infrared Spectroscopy. Infrared spectra were recorded on a Matterson FTIR 5000 spectrometer in the 400−4000 cm^{-1} range.

UV−vis Diffuse Reflectance Spectroscopy. UV−visible diffuse reflectance data for the reported compounds were collected on a Varian Cary 500 scan UV−vis-NIR spectrophotometer over the spectral range 200−1500 nm at room temperature. Poly(tetrafluoroethylene) (PTFE) was used as a reference material. Reflectance spectra were converted to absorbance using the Kubelka−Munk function.[42,43]

(36) *SAINT; A Program for Area Detector Absorption Correction*, Version 4.05; Siemens Analytical X-ray Systems, Inc.: Madison, WI, 1995.
(37) Sheldrick, G. M. *SHELXS-97: A program for automatic solution of crystal structures*., University of Goettingen: Goettingen, Germany, 1997.
(38) Sheldrick, G. M. *SHELXL-97: A program for crystal structure refinement*; University of Goettingen: Goettingen, Germany, 1997.
(39) Sheldrick, G. M. *SHELXTL DOS/Windows/NT*, Version 5.10; Bruker Analytical X-Ray Instruments, Inc.: Madison, WI, 1997.
(40) Farrugia, L. J. *J. Appl. Crystallogr.* **1999**, *32*, 837.
(41) Spek, A. L. *PLATON*; Utrecht University: Utrecht, The Netherlands, 2001.
(42) Kubelka, P.; Munk, F. *Z. Tech. Phys.* **1931**, *12*, 593.
(43) Tauc, J. *Mater. Res. Bull.* **1970**, *5*, 721.

Table 1. Crystallographic Data for $Rb_2(MoO_3)_3(SeO_3)$ and $Tl_2(MoO_3)_3(SeO_3)$

parameter	$Rb_2(MoO_3)_3(SeO_3)$	$Tl_2(MoO_3)_3(SeO_3)$
formula weight, fw	729.72	967.52
T	296.0(2) K	296.0(2) K
λ	0.71073 Å	0.71073 Å
crystal system	hexagonal	trigonal
space group	$P6_3$ (No. 173)	$P\bar{3}1c$ (No. 159)
a	7.2992(14) Å	7.2867(10) Å
b	7.2992(14) Å	7.2867(10) Å
c	11.978(5) Å	11.794(3) Å
α	90°	90°
β	90°	90°
γ	120°	120°
V	552.7(3) Å^3	542.33(18) Å^3
Z	2	2
calculated density, ρ_{calcd}	4.385 g/cm^3	5.925 g/cm^3
μ	15.453 mm^{-1}	36.398 mm^{-1}
$2\theta_{max}$	57.82°	57.70°
Flack parameter	0.017(9)	0.023(11)
goodness of fit, GOF	1.054	1.059
$R(F)^a$	0.0217	0.0327
$R_w(F_o^2)^b$	0.0551	0.0717

$^a R(F) = \sum||F_o| - |F_c||/\sum|F_o|$. $^b R_w(F_o^2) = [\sum w(F_o^2 - F_c^2)^2/\sum w(F_o^2)^2]^{1/2}$.

Table 2. Atomic Coordinates for $Rb_2(MoO_3)_3(SeO_3)$ and $Tl_2(MoO_3)_3(SeO_3)$

atom	x	y	z	U_{eq} (Å^2)^a
		$Rb_2(MoO_3)_3(SeO_3)$		
Rb(1)	0.6667	0.3333	0.05749(9)	0.0393(3)
Rb(2)	0.3333	0.6667	0.93194(7)	0.0228(2)
Mo(1)	0.33987(5)	0.13343(5)	0.76926(3)	0.00851(13)
Se(1)	0.0000	0.0000	0.00052(6)	0.00964(17)
O(1)	0.4083(6)	0.2026(6)	0.6328(3)	0.0157(7)
O(2)	0.2460(5)	0.1271(5)	0.9403(3)	0.0148(6)
O(3)	0.5465(5)	0.0857(5)	0.8171(3)	0.0134(6)
O(4)	0.1234(4)	0.8697(4)	0.7551(3)	0.0136(6)
		$Tl_2(MoO_3)_3(SeO_3)$		
Tl(1)	0.3333	0.6667	0.34467(11)	0.0561(4)
Tl(2)	0.6667	0.3333	0.22930(6)	0.0271(3)
Mo(1)	0.33987(12)	0.13365(13)	0.56590(8)	0.0072(2)
Se(1)	0.0000	0.0000	0.30084(17)	0.0085(3)
O(1)	0.4102(12)	0.2049(13)	0.4276(6)	0.0128(15)
O(2)	0.2429(11)	0.1235(12)	0.7402(6)	0.0102(15)
O(3)	0.5462(11)	0.853(11)	0.6156(7)	0.0121(15)
O(4)	0.1210(12)	0.8680(12)	0.5506(8)	0.0119(14)

$^a U_{eq}$ is defined as one-third of the trace of the orthogonalized U_{ij} tensor.

Thermogravimetric Analysis. Thermogravimetric analyses were performed on a Model TGA 951 thermogravimetric analyzer (TA Instruments). The sample was placed in a platinum crucible and heated at a rate of 10 °C/min from room temperature to 800 °C under flowing nitrogen.

Differential Scanning Calorimetry. Differential scanning calorimetry (DSC) analysis was performed using a Model EX-STAR 6000 differential scanning calorimeter (SII Nano Technology, Inc.). The sample was placed in an aluminum pan covered with an aluminum lid that was heated (cooled) at a rate of 10 °C/min from 25 °C to 280 °C under flowing air. Alumina was used during the measurements as a reference. No endothermic or exothermic peaks were observed.

Second Harmonic Generation. Powder SHG measurements were performed on a modified Kurtz-NLO system,[44] using a pulsed Nd:YAG laser with a wavelength of 1064 nm. A detailed description of the equipment and methodology has been published.[45] SHG efficiency has been shown to be strongly dependent on particle size;[44] thus, polycrystalline samples were ground and sieved into distinct particle size ranges (20−45, 45−63, 63−75, 75−90, 90−120, >120 μm). Crystalline α-SiO_2 was also ground and sieved into the same particle size ranges, to make relevant comparisons with known SHG materials. No index matching fluid was used in any of the experiments.

Table 3. Selected Bond Distances for $Rb_2(MoO_3)_3(SeO_3)$ and $Tl_2(MoO_3)_3(SeO_3)$

$Rb_2(MoO_3)_3(SeO_3)$		$Tl_2(MoO_3)_3(SeO_3)$	
bond	distance (Å)	bond	distance (Å)
Rb(1)−O(2) × 3	3.007(3)	Tl(1)−O(2) × 3	2.944(7)
Rb(1)−O(3) × 3	3.278(4)	Tl(1)−O(3) × 3	3.123(8)
Rb(1)−O(4) × 3	3.524(3)	Tl(1)−O(4) × 3	3.566(9)
Rb(2)−O(1) × 3	2.908(4)	Tl(2)−O(1) × 3	2.844(7)
Rb(2)−O(3) × 3	2.985(3)	Tl(2)−O(3) × 3	2.963(7)
Rb(2)−O(4) × 3	3.362(3)	Tl(2)−O(4) × 3	3.355(8)
Mo(1)−O(1)	1.709(4)	Mo(1)−O(1)	1.711(7)
Mo(1)−O(2)	2.154(3)	Mo(1)−O(2)	2.163(7)
Mo(1)−O(3)	1.803(3)	Mo(1)−O(3)	1.805(7)
Mo(1)−O(3)	2.122(3)	Mo(1)−O(3)	2.123(7)
Mo(1)−O(4)	1.786(3)	Mo(1)−O(4)	1.799(8)
Mo(1)−O(4)	2.117(3)	Mo(1)−O(4)	2.098(8)
Se(1)−O(2) × 3	1.714(3)	Se(1)−O(2) × 3	1.692(7)

Piezoelectric and Polarization Measurements. Piezoelectric measurements were performed using a Radiant Technologies Model RT66A piezoelectric test system with a TREK high-voltage amplifier (Model 609E-6), Precision materials analyzer, Precision high-voltage interface, and MTI 2000 photonic sensor. A maximum voltage of 500 V was applied to the samples. With each sample, 20 measurements were performed and an average was taken. The polarization was measured on a Radiant Technologies Model RT66A ferroelectric test system with a TREK high-voltage amplifier between room temperature and 150 °C in a Delta Model 9023 environmental test chamber. The unclamped pyroelectric coefficient, defined as dP/dT (the change in the polarization, with respect to the change in temperature) was determined by measuring the polarization as a function of temperature. A detailed description of the methodology used has been published elsewhere.[45] The samples were pressed into pellets (~12 mm diameter, ~1 mm thick) and sintered, well below the decomposition temperatures, at 280 °C for 10 h for all three materials: $Rb_2(MoO_3)_3(SeO_3)$, $Cs_2(MoO_3)_3(SeO_3)$, and $Tl_2(MoO_3)_3(SeO_3)$. Silver paste was applied to both sides as electrodes and cured at 200 °C for 3 h. To measure the potential ferroelectric behavior, polarization measurements were done at room temperature under a static electric field of 15 kV/cm at various frequencies (10, 20, 50, and 100 Hz). For the pyroelectric measurements, the polarization was measured statically from room temperature to 145 °C in 20 °C increments, with an electric field of 9 kV/cm. The temperature was allowed to stabilize before the polarization was measured.

Results

Structures. Although $Rb_2(MoO_3)_3(SeO_3)$ and $Tl_2(MoO_3)_3(SeO_3)$ are structurally very similar, the materials crystallize in different space groups: $P6_3$ and $P\bar{3}1c$, respectively. Both materials exhibit layered hexagonal tungsten oxide (HTO)-type topologies, consisting of corner-shared

(44) Kurtz, S. K.; Perry, T. T. *J. Appl. Phys.* **1968**, *39*, 3798.

(45) Ok, K. M.; Chi, E. O.; Halasyamani, P. S. *Chem. Soc. Rev.* **2006**, *35*, 710.

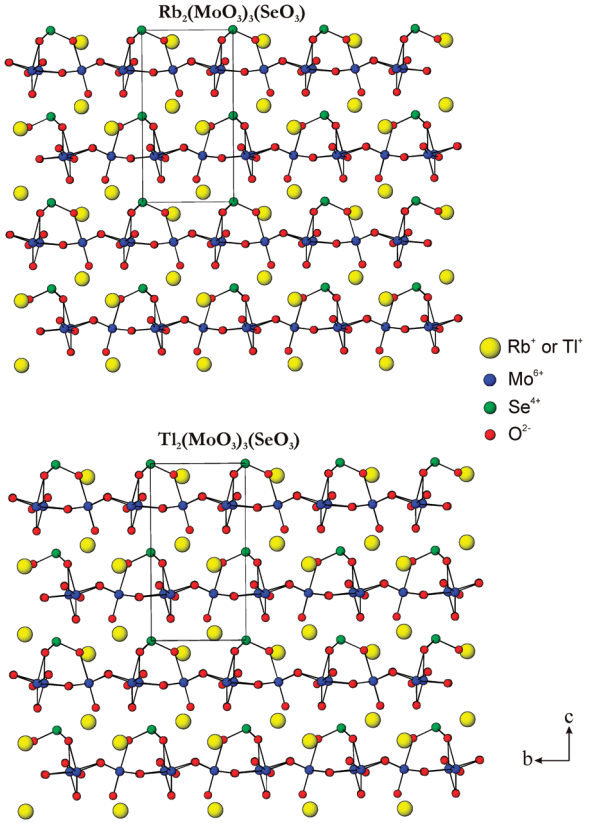

Figure 3. Ball-and-stick diagram of $Rb_2(MoO_3)_3(SeO_3)$ (top) and $Tl_2(MoO_3)_3(SeO_3)$ (bottom) in the *bc*-plane. Note that the coordination environment of the Rb^+ and Tl^+ cations are identical, indicating that the lone pair on Tl^+ is inert, as opposed to stereoactive.

MoO_6 octahedra that are "capped" on one side by SeO_3 polyhedra (i.e., Class 2 HTOs). The layers are separated by Rb^+ or Tl^+ cations (see Figure 3). Each MoO_6 octahedron is linked to two additional MoO_6 octahedra and one SeO_3 polyhedron through oxide bonds. In connectivity terms, the structure may be written as $\{3[MoO_{1/1}O_{5/2}]^-[SeO_{3/2}]^+\}^{2-}$, with charge balance maintained by two Rb^+ or two Tl^+ cations. In the *ab*-plane, the MoO_6 and SeO_3 polyhedral connectivity produces puckered rings, where the Rb^+ or Tl^+ cations reside (see Figure 4). The Mo−O and Se−O bonds distances for $Rb_2(MoO_3)_3(SeO_3)$ ($Tl_2(MoO_3)_3(SeO_3)$) are in the range of 1.709(4)−2.154(3) Å (1.711(7)−2.163(7) Å) and 1.714(3) Å (1.692(7) Å), respectively. The Rb^+ and Tl^+ cations are in nine-coordinate oxide environments with bond distances in the range of 2.844(7)−3.566(9) Å. The similar coordination environments suggest that the lone pair on Tl^+ may be described as inert rather than stereoactive.[46,47] A complete list of bond lengths is given in Table 3. Bond valence calculations[48,49] resulted in values of 0.69−1.11, 0.78−1.03, 3.90−4.14, and 6.01−6.06 for Rb^+, Tl^+, Se^{4+}, and Mo^{6+}, respectively. Both the Mo^{6+} and Se^{4+} cations are in asymmetric coordination environments attributable to

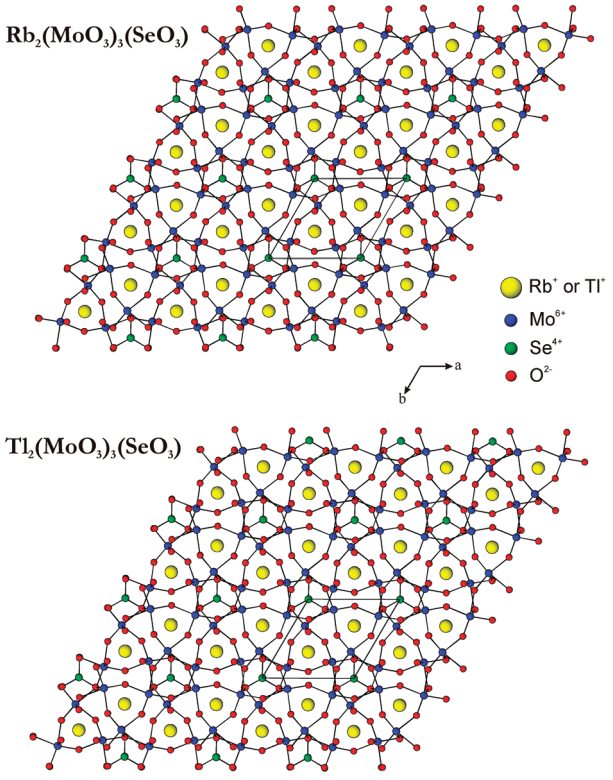

Figure 4. Ball-and-stick diagram of $Rb_2(MoO_3)_3(SeO_3)$ (top) and $Tl_2(MoO_3)_3(SeO_3)$ (bottom) in the *ab*-plane.

second-order Jahn−Teller (SOJT) effects.[50−57] With the Mo^{6+} cation, an out-of-center distortion toward the face of the oxide octahedron is observed, whereas for the Se^{4+} cation, a stereoactive lone pair is found, resulting in the observed asymmetric coordination environment (see Figure 5). A face, or C_3-type, distortion for Mo^{6+} in $Rb_2(MoO_3)_3(SeO_3)$ ($Tl_2(MoO_3)_3(SeO_3)$) results in three "short" (1.709(4)−1.803(3) Å (1.711(7)−1.805(7) Å)) and three "long" (2.098(8)−2.163(7) Å (2.098(8)−2.163(7) Å)) Mo−O bonds, respectively. In addition, using continuous symmetry measurers,[58,59] we were able to quantify the magnitude of the out-of-center distortion for the Mo^{6+} cation.[60] The magnitudes are 0.112 and 0.110 $Å^2$ for $Rb_2(MoO_3)_3(SeO_3)$ and $Tl_2(MoO_3)_3(SeO_3)$, respectively, which are consistent with those reported earlier.[61]

Infrared Spectroscopy. The infrared spectra for $Rb_2(MoO_3)_3(SeO_3)$ and $Tl_2(MoO_3)_3(SeO_3)$ revealed Mo−O and Se−O vibrations between 500 and 1000 cm^{-1}. The stretches, in the 600−800 cm^{-1} range, can be attributed

(46) Stoltzfus, M. W.; Woodward, P.; Seshadri, R.; Park, J.-H.; Bursten, B. *Inorg. Chem.* **2007**, *46*, 3839.
(47) Yeon, J.; Kim, S.-H.; Halasyamani, P. S. *J. Solid State Chem.* **2009**, *182*, 3269.
(48) Brown, I. D.; Altermatt, D. *Acta Crystallogr., Sect. B: Struct. Sci.* **1985**, *B41*, 244.
(49) Brese, N. E.; O'keeffe, M. *Acta Crystallogr., Sect. B: Struct. Sci.* **1991**, *B47*, 192.
(50) Opik, U.; Pryce, M. H. L. *Proc. R. Soc. London, Ser. A* **1957**, *238*, 425.
(51) Bader, R. F. W. *Mol. Phys.* **1960**, *3*, 137.
(52) Bader, R. F. W. *Can. J. Chem.* **1962**, *40*, 1164.
(53) Pearson, R. G. *J. Am. Chem. Soc.* **1969**, *91*, 4947.
(54) Pearson, R. G. *J. Mol. Struct.:THEOCHEM* **1983**, *103*, 25.
(55) Wheeler, R. A.; Whangbo, M. H.; Hughbanks, T.; Hoffmann, R.; Burdett, J. K.; Albright, T. A. *J. Am. Chem. Soc.* **1986**, *108*, 2222.
(56) Kunz, M.; Brown, I. D. *J. Solid State Chem.* **1995**, *115*, 395.
(57) Goodenough, J. B. *Annu. Rev. Mater. Sci.* **1998**, *28*, 1.
(58) Zabrodsky, H.; Peleg, S.; Avnir, D. *J. Am. Chem. Soc.* **1992**, 114.
(59) Alvarez, S.; Alemany, P.; Avnir, D. *Chem. Soc. Rev.* **2005**, *34*, 313.
(60) Llunell, M.; Casanova, D.; Cirera, J.; Bofill, J. M.; Alemany, P.; Alvarez, S.; Pinsky, M.; Avnir, D. *Shape Program, version 1.1b, 1.1b*; University of Barcelona: Barcelona, Spain, 2004.
(61) Ok, K. M.; Halasyamani, P. S.; Casanova, D.; Llunell, M.; Alemany, P.; Alvarez, S. *Chem. Mater.* **2006**, *18*, 3176.

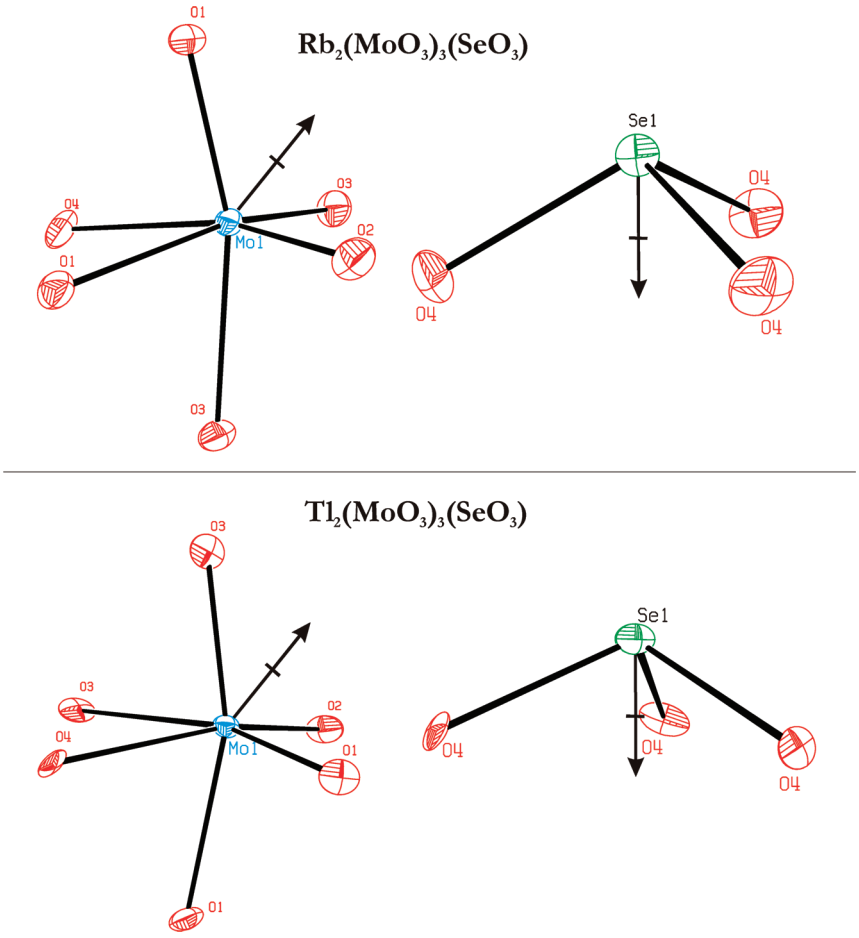

Figure 5. ORTEP (50% probability ellipsoids) of the MoO_6 and SeO_3 polyhedra in $Rb_2(MoO_3)_3(SeO_3)$ (top) and $Tl_2(MoO_3)_3(SeO_3)$ (bottom). The approximate direction of the dipole moments are also shown (black arrows).

to Mo−O vibrations, whereas the stretches in the 1000−800 cm^{-1} range are related to Se−O vibrations. The assignments are consistent with those previously reported (see Figure S4 in the Supporting Information).[25,27,62]

UV−vis Diffuse Reflectance Spectroscopy. The UV−vis diffuse reflectance spectra indicate that the absorption energy for $Rb_2(MoO_3)_3(SeO_3)$, $Cs_2(MoO_3)_3(SeO_3)$, and $Tl_2(MoO_3)_3(SeO_3)$ is ~3.0 eV. Absorption (K/S) data were calculated from the Kubelka−Munk function:[42]

$$F(R) = \frac{(1-R)^2}{2R} = \frac{K}{S}$$

with R, K, and S representing the reflectance, absorption, and scattering, respectively. In a plot of K/S versus E (eV), extrapolating the linear part of the rising curve to zero provides the onset of absorption at 3.2, 3.1, and 3.0 eV for $Rb_2(MoO_3)_3(SeO_3)$, $Cs_2(MoO_3)_3(SeO_3)$, and $Tl_2(MoO_3)_3(SeO_3)$, respectively (see Figure S5 in the Supporting Information).

Thermogravimetric Analysis. The thermal behavior of $Rb_2(MoO_3)_3(SeO_3)$ and $Tl_2(MoO_3)_3(SeO_3)$ was investigated using thermogravimetric analysis (TGA). The TGA curve for $Rb_2(MoO_3)_3(SeO_3)$ reveals a single-step decomposition from 300 °C to 500 °C, attributable to the sublimation of 1 mol of SeO_2, exp. (calc.) 83.62% (84.79%), resulting in the formation of $Rb_2Mo_3O_{10}$ (see Figure S6 in the Supporting Information). For $Tl_2(MoO_3)_3(SeO_3)$, the TGA curve also shows a single-step decomposition from 300 °C to 400 °C, attributable to the sublimation of 1 mol of SeO_2, exp. (calc.) 88.61% (88.53%) (see Figure S6 in the Supporting Information). A mixture of Tl_2MoO_4, MoO_3, and $Tl_2Mo_3O_{10}$ was confirmed by powder XRD.

Functional Inorganic Properties: Second Harmonic Generation, Piezoelectricity, and Polarization Measurements. With the reported materials and $Cs_2(MoO_3)_3(SeO_3)$, Table 4 lists their bond valence sums, SHG efficiencies, piezoelectric coefficient, pyroelectric constant, and maximum polarization. The materials, $Rb_2(MoO_3)_3(SeO_3)$ and $Cs_2(MoO_3)_3(SeO_3)$, as well as $Tl_2(MoO_3)_3(SeO_3)$, crystallize in polar noncentrosymmetric (NCS) space groups, $P6_3$ (Rb and Cs compounds) or $P31c$ (Tl compounds). Powder SHG measurements using 1064-nm radiation revealed SHG efficiencies of 300, 350, and 400 × α-SiO_2 for $Rb_2(MoO_3)_3(SeO_3)$, $Cs_2(MoO_3)_3(SeO_3)$, and $Tl_2(MoO_3)_3(SeO_3)$, respectively. Thus, there is very little change in the SHG efficiency with respect to the A cation (A = Rb^+, Cs^+, or Tl^+), indicating that the lone pair on Tl^+ is inert, rather than stereoactive. SHG measurements on sieved particles in the 20−140 μm range indicated that all

(62) Dussack, L. L.; Harrison, W. T. A.; Jacobson, A. J. *Mater. Res. Bull.* **1996**, *31*, 249.

Table 4. Bond Valence Sum (BVS), SHG Efficiency, Piezoelectric Response, Pyroelectric Coefficient, and Maximum Polarization (P_m) for $A_2(MoO_3)_3(SeO_3)$ (A = Rb, Cs, and Tl)

	Bond Valence Sum, BVS							
compound	$A^+(1)$	$A^+(2)$	Mo^{6+}	Se^{4+}	SHG efficiency (× α-SiO_2)	piezoelectric response, d_{33} (pm/V)	pyroelectric coefficient @ 45 °C ($\mu C/m^2K$)	maximum polarization, P_m @10 Hz ($\mu C/cm^2$)
$Rb_2(MoO_3)_3(SeO_3)$	0.69	1.11	6.06	3.90	300	9	−1.1	0.08
$Cs_2(MoO_3)_3(SeO_3)$	0.75	1.38	6.05	3.89	350	11	−2.0	0.13
$Tl_2(MoO_3)_3(SeO_3)$	0.78	1.03	6.01	4.14	400	13	−2.1	0.11

of the materials are non-phase-matchable (see Figure S8 in the Supporting Information). Based on the SHG efficiencies and phase-matching measurements, the materials fall into the Class C category of SHG materials.[44] The phase-matching measurements also allow us to estimate $\langle d_{eff} \rangle$, which is the average NLO susceptibility for the materials.[28,45] For $Rb_2(MoO_3)_3(SeO_3)$, $Cs_2(MoO_3)_3(SeO_3)$, and $Tl_2(MoO_3)_3(SeO_3)$, the $\langle d_{eff} \rangle$ values are ∼9.6, ∼10.7, and ∼11.7 pm/V, respectively. Converse piezoelectric measurements were also performed that revealed approximate d_{33} values of 9, 11, and 13 pm/V for $Rb_2(MoO_3)_3(SeO_3)$, $Cs_2(MoO_3)_3(SeO_3)$, and $Tl_2(MoO_3)_3(SeO_3)$, respectively (see Figure S9 in the Supporting Information and Table 4). Because the materials are polar, the pyroelectric coefficient was determined by measuring the spontaneous polarization (P_s) as a function of temperature (see Figure S10 in the Supporting Information). The values of the pyroelectric coefficient, which is defined as $p = dP_s/dT$, for $Rb_2(MoO_3)_3(SeO_3)$, $Cs_2(MoO_3)_3(SeO_3)$, and $Tl_2(MoO_3)_3(SeO_3)$ at 45 °C are −1.1, −2.0, and −2.1 $\mu C\ m^{-2}\ K^{-1}$, respectively (see Figure S10 in the Supporting Information). The magnitudes of these coefficients are consistent with other known pyroelectric materials, e.g., ZnO (−9.4 $\mu C\ m^{-2}\ K^{-1}$) and tourmaline (−4.0 $\mu C\ m^{-2}\ K^{-1}$).[63] All of the materials discussed are not only noncentrosymmetric (NCS) but also are polar, i.e., exhibit a macroscopic dipole moment. Measurements were performed to determine if the dipole moment was reversible, or switchable. Although "hysteresis loops" were observed, the reported materials, as well as $Cs_2(MoO_3)_3(SeO_3)$, are not ferroelectric. In other words, the macroscopic polarization is not switchable. The loops are attributable to dielectric loss and not ferroelectric hysteresis (see Figure S11 in the Supporting Information).[64] Macroscopic polarization reversibility implies microscopic, or local, polarization reversibility. Although it is straightforward to visualize the local dipole moment of Mo^{6+} being switched from one face to the opposite without any substantial rearrangement or breaking of bonds, the dipole moment associated with Se^{4+} cannot be inverted. For this polarization to be reversed, the entire SeO_3 polyhedron must be inverted. This is not possible without substantial bond rearrangements and/or bond breaking. In addition, we have previously demonstrated that polarization inversion of a SeO_3 polyhedron is energetically very unfavorable.[22] Thus, it is not surprising that ferroelectric behavior with fourth and fifth period cations (Se^{4+}, Te^{4+}, etc.), where the polarization is "flipped", has never been observed.

Discussion

In addition to reporting on the synthesis and characterization of two new polar oxides, one of the objectives of this paper was to discuss polar HTO-type oxides, as a whole, to better understand their functional properties and structure−property relationships. We have divided the polar HTOs into two classes: Class 1 and Class 2. With the Class 1 materials, the corner-shared octahedral layers are "capped" on both sides by lone-pair polyhedra or methyl-phosphate groups, whereas with the Class 2 HTOs, the analogous layers are "capped" on only one side (see Figures 2a and b). In Table 5, we list all known polar HTO materials, along with their space group and other distortion parameters. We will be discussing these parameters in more detail. The Class 1 HTOs may be written in general connectivity terms as $\{A^+[3(MO_{6/2})^-(LO_{3/2})^+(L'O_{3/2})^+]\}^0$, where $A^+ = K^+, Rb^+, Cs^+, Tl^+$, or NH_4^+; $M = V^{5+}$; L, L′ = Se^{4+}, Te^{4+}, or $(P\text{-}CH_3)^{4+}$. Using both L and L′ is necessary, because the layers are "capped" on both sides by LO_3 and $L'O_3$ polyhedra. With the Class 2 HTOs, the materials may be described as $\{2A^+[3(MO_{1/1}O_{5/2})^-(LO_{3/2})^+]\}^0$, where $A^+ = Rb^+, Cs^+, Tl^+$, or NH_4^+; $M = Mo^{6+}$ or W^{6+}; L = Se^{4+}, Te^{4+}, or $(P\text{-}CH_3)^{4+}$.

A major nonstructural difference between the Class 1 and Class 2 HTOs is the d^0 transition-metal cation. For Class 1 HTOs, V^{5+} is exclusively observed, whereas for the Class 2 HTOs, both Mo^{6+} and W^{6+} are found. As we will demonstrate, the specific d^0 transition metal profoundly impacts the direction and magnitude of the intraoctahedral distortion. With the V^{5+} cations in the Class 1 HTOs, the displacement is toward an edge, i.e., a C_2-type distortion (see Table 5). We have previously demonstrated that, for oxides with VO_6 octahedra and lone-pair polyhedra, the most common V^{5+} displacement is toward a corner, i.e., C_4-type.[65] If we examine Figure 6a, we can better understand why a C_2-type distortion is observed with the Class 1 HTOs. As seen in Figure 6a, the VO_6 octahedron is "capped" above and below by a SeO_3 polyhedron (L and L′, referenced above). For materials that contain both an octahedrally coordinated d^0 cation and a lone-pair metal, we demonstrated previously that the displacement of the d^0 cation will be in a direction *away from* the oxide ligand that also bonds to the lone-pair cation.[66] This is attributable to

(63) Lang, S. B. *Phys. Today* **2005**, *58*, 31.
(64) Scott, J. F. *J. Phys.: Condens. Matter* **2008**, *20*, 021001.
(65) Ok, K. M.; Halasyamani, P. S.; Casanova, D.; Llunell, M.; Alemany, P.; Alvarez, S. *Chem. Mater.* **2006**, *18*, 3176.
(66) Halasyamani, P. S. *Chem. Mater.* **2004**, *16*, 3586.

Table 5. Classification, Space Group, Distortion Direction of the d^0 Cation, Magnitude of Distortion for the d^0 Cation (Δ_d), Bond Strain Index (BSI), Global Instability Index (GII), and Dipole Moments Magnitudes for d^0 and Lone-Pair Cations

compound	space group	distortion direction	Δ_d[a] (Å^2)	Dipole Moment MO_6[b]	Dipole Moment LO_3[c]	Dipole Moment $L'O_3$[d]	BSI (vu)[e]	GII (vu)[e]
			Class 1 Classification					
$(NH_4)(VO_2)_3(SeO_3)_2$[19]	$P6_3$	C_2	0.127	9.0	7.7	6.4	0.199	0.068
$K(VO_2)_3(SeO_3)_2$[20]	$P6_3$	C_2	0.134	9.3	7.3	6.6	0.195	0.112
$Rb(VO_2)_3(SeO_3)_2$[22]	$P6_3$	C_2	0.135	9.4	7.4	7.0	0.197	0.111
$Cs(VO_2)_3(SeO_3)_2$[21]	$P6_3$	C_2	0.130	9.0	6.5	7.1	0.189	0.086
$Tl(VO_2)_3(SeO_3)_2$[22]	$P6_3$	C_2	0.121	8.9	7.2	6.6	0.180	0.092
$Cs(VO_2)_3(TeO_3)_2$[23]	$P6_3$	C_2	0.134	9.0	9.5	9.6	0.189	0.066
$(NH_4)(VO_2)_3(PO_3CH_3)_2$[24]	$R32$	C_2	0.121	8.2	6.4	6.4	0.135	0.018
$K(VO_2)_3(PO_3CH_3)_2$[24]	$R32$	C_2	0.125	8.1	6.4	6.4	0.132	0.036
			Class 2 Classification					
$(NH_4)_2(MoO_3)_3(SeO_3)$[25]	$P6_3$	C_3	0.108	5.2	7.1	[f]	0.138	0.113
$Rb_2(MoO_3)_3(SeO_3)$[g]	$P6_3$	C_3	0.112	5.1	6.3		0.134	0.090
$Cs_2(MoO_3)_3(SeO_3)$[25]	$P6_3$	C_3	0.096	4.0	5.7		0.130	0.123
$Tl_2(MoO_3)_3(SeO_3)$[g]	$R31c$	C_3	0.110	5.3	5.3		0.128	0.074
$(NH_4)_2(MoO_3)_3(TeO_3)$[26]	$P6_3$	C_3	0.109	5.5	8.9		0.143	0.086
$Cs_2(MoO_3)_3(TeO_3)$[26]	$P6_3$	C_3	0.102	6.3	9.3		0.146	0.140
$(NH_4)_2(WO_3)_3(SeO_3)$[27]	$P6_3$	C_3	0.040	3.6	7.5		0.106	0.142
$Cs_2(WO_3)_3(SeO_3)$[27]	$P6_3$	C_3	0.072	4.1	6.0		0.101	0.147
$Rb_2(WO_3)_3(TeO_3)$[28]	$R31c$	C_3	0.061	4.0	8.5		0.139	0.151
$Rb_2(MoO_3)_3(PO_3CH_3)$[20]	$R3$	C_3	0.113	5.2	6.5		0.123	0.102
$Cs_2(MoO_3)_3(PO_3CH_3)$[20]	$R3$	C_3	0.116	5.5	6.7		0.121	0.136
$Tl_2(MoO_3)_3(PO_3CH_3)$[30]	$R3$	C_3	0.109	5.2	5.9		0.120	0.082
$Cs_2(WO_3)_3(PO_3CH_3)$[31]	$R3$	C_2	0.077	4.2	5.9		0.106	0.137

[a] Magnitude of the out-of-center distortion for MO_6 (M = V^{5+}, Mo^{6+}, or W^{6+}). [b] Local dipole moments for MO_6. [c] Local dipole moments for "capping" polyhedra (L = Se^{4+}, Te^{4+}, or P^{3+}-CH_3). [d] Local dipole moments for "capping" polyhedra (L′ = Se^{4+}, Te^{4+}, or P^{3+}-CH_3). [e] The abbreviation "vu" denotes valence unit. [f] Class 2 compounds have only one "capping" polyhedron. [g] This work.

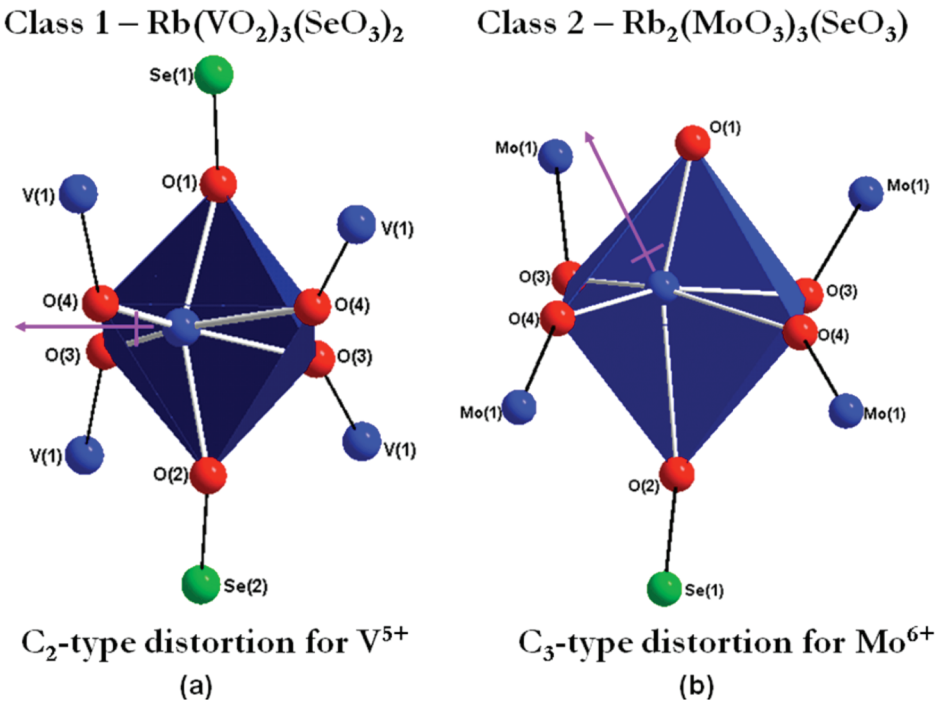

Figure 6. (a) Primary and secondary coordination of the V^{5+} cation in the Class 1 HTO $Rb(VO_2)_3(SeO_3)_2$. (b) Primary and secondary coordination of the Mo^{6+} cation in the Class 2 HTO $Rb_2(MoO_3)_3(SeO_3)$. In both panels (a) and (b), the direction of the d^0 cation distortion (denoted by the purple arrow) is away from the oxide ligand bridging to the lone-pair cation (green sphere).

the predistorted nature of the lone-pair polyhedron, i.e., the lone-pair cation cannot undergo any additional displacement, because its coordination is already highly asymmetric.[66] Thus, with the Class 1 HTOs, the V^{5+} cation cannot distort toward a corner, toward either oxide ligand bonded to the Se^{4+} cation, and is forced to displace toward an edge, i.e., a C_2-type displacement. An analogous situation occurs with the Class 2 HTOs. With these materials, octahedrally coordinated Mo^{6+} and W^{6+} are both observed. Of the 13 examples of Class 2 HTOs, a face or C_3-type displacement is observed in 12 of them, with an edge or C_2-type in the remaining example (see

Table 5). The local and secondary coordination of a MoO_6 octahedron in a Class 2 HTO is shown in Figure 6b. Unlike the Class 1 HTOs, for the Class 2 HTOs, the lone-pair polyhedron only "caps" one side. In addition, the oxide opposite to the lone-pair is terminal; see the $O_{1/1}$ in the connectivity formula above. In materials that contain MoO_6 or WO_6 octahedra and a lone-pair polyhedra, a distortion toward a corner, C_4-type, has never been observed with Mo^{6+} and is extremely rare for W^{6+}.[65] Thus, for the Class 2 HTOs, a distortion toward a corner does not occur; instead, the Mo^{6+} and W^{6+} cations are displaced toward a face (i.e., C_3-type distortion) that is common for both Mo^{6+} and W^{6+}.

In addition to the differences in the direction of the distortion, the magnitudes also differ between the Class 1 and Class 2 HTOs. Using continuous measurers and the Shape program,[60,67−69] we were able to determine the magnitude of the d^0 transition-metal displacement for all the HTOs (see Table 5). For the Class 1 HTOs, the V^{5+} displacement average is 0.128 Å^2, which is slightly smaller than the 0.145 Å^2 average determined earlier.[66] The Class 2 HTOs contain both Mo^{6+} and W^{6+} cations. The average displacement magnitudes for Mo^{6+} and W^{6+} are 0.108 and 0.063 Å^2, respectively. The latter is very similar to the average reported earlier for W^{6+} (0.062 Å^2), whereas the former is substantially smaller than the reported average of 0.158 Å^2.[66] The most prevalent displacement direction for the Mo^{6+} is a C_2-type, i.e., toward an edge. With a C_2-type distortion, the cation displaces toward two oxide ligands, as opposed to three with a C_3-type distortion. Displacing toward two ligands allows the cation to distort further (i.e., larger magnitude), compared to three ligands. Thus, for the Class 2 HTOs that contain Mo^{6+}, the magnitude of the displacement is smaller than normally observed. The magnitudes of the d^0 cation displacement correlates with the magnitude of the dipole moment associated with the MO_6 octahedron (where M is the d^0 cation). In other words, the magnitude of the dipole moments for the Class 1 HTOs MO_6 octahedra are larger than the Class 2 HTOs, because the d^0 cation displacement is larger for Class 1, compared to Class 2. The dipole moment magnitudes with the lone-pair and methyl phosphonate polyhedra are fairly similar across both classes (see Table 5).

The final two distortion parameters that we used to better understand the HTOs are the bond strain index (BSI) and the global instability index (GII).[70−72] Both indices can be used to determine the extent of the lattice and electronically induced strain in any structure. Except for four materials, with the Class 1 and Class 2 HTOs, the BSI value is greater than the GII value, indicating that the electronically induced strain (i.e., SOJT effects) are larger than the lattice-induced strain. The four materials where the GII value is greater than the BSI value are $(NH_4)_2(WO_3)_3(SeO_3)$,[27] $Cs_2(WO_3)_3(SeO_3)$,[27] $Rb_2(WO_3)_3(TeO_3)$,[28] and $Cs_2(WO_3)_3(PO_3CH_3)$.[31] All of the materials are Class 2 HTOs and contain W^{6+}. The magnitudes of the displacements for the W^{6+} cation in these materials are < 0.08 Å^2. Thus, the electronically induced strain is weak, which results in a low BSI value. However, the materials still exhibit a sizable lattice strain that is reflected in the larger GII value. It is illustrative if we compare the distortion magnitudes (the BSI and GII values) of two sets of isostructural materials, specifically, $(NH_4)_2(MoO_3)_3(SeO_3)$/$(NH_4)_2(WO_3)_3(SeO_3)$ and $Cs_2(MoO_3)_3(SeO_3)$/$Cs_2(WO_3)_3(SeO_3)$.

compound	Δ_d (Å^2)	BSI (vu)[a]	GII (vu)[a]
$(NH_4)_2(MoO_3)_3(SeO_3)$[25]	0.108	0.138	0.113
$(NH_4)_2(WO_3)_3(SeO_3)$[27]	0.040	0.106	0.142
$Cs_2(MoO_3)_3(SeO_3)$[25]	0.096	0.130	0.123
$Cs_2(WO_3)_3(SeO_3)$[27]	0.072	0.101	0.147

[a] The abbreviation "vu" denotes valence unit.

As seen, the magnitude of the d^0 metal distortion is substantially larger for the molybdates, compared to the tungstates. As such, for the molybdates, BSI > GII, whereas for the tungstates, GII > BSI. Therefore, with the molybdates, the electronically induced strain is greater than the lattice-induced strain, whereas for the tungstates, the lattice-induced strain is greater than the electronically induced strain.

Finally, we compare the powder SHG for all the HTOs (see Table 6). For many of the materials listed in Table 6,

Table 6. Powder SHG Efficiencies for Class 1 and Class 2 HTO-Type Materials

compound	SHG (× α-SiO_2)
Class 1 Classification	
$(NH_4)(VO_2)_3(SeO_3)_2$[19]	40
$K(VO_2)_3(SeO_3)_2$[20]	45
$Rb(VO_2)_3(SeO_3)_2$[22]	40
$Cs(VO_2)_3(SeO_3)_2$[21]	40
$Tl(VO_2)_3(SeO_3)_2$[22]	50
$Cs(VO_2)_3(TeO_3)_2$[23]	40
$(NH_4)(VO_2)_3(PO_3CH_3)_2$[24]	30
$K(VO_2)_3(PO_3CH_3)_2$[24]	30
Class 2 Classification	
$(NH_4)_2(MoO_3)_3(SeO_3)$[25]	400
$Rb_2(MoO_3)_3(SeO_3)$[a]	300
$Cs_2(MoO_3)_3(SeO_3)$[25]	350
$Tl_2(MoO_3)_3(SeO_3)$[a]	400
$(NH_4)_2(MoO_3)_3(TeO_3)$[26]	400
$Cs_2(MoO_3)_3(TeO_3)$[26]	400
$(NH_4)_2(WO_3)_3(SeO_3)$[27]	200
$Cs_2(WO_3)_3(SeO_3)$[27]	200
$Rb_2(WO_3)_3(TeO_3)$[28]	200
$Cs_2(WO_3)_3(TeO_3)$[28]	400
$Cs_2(MoO_3)_3PO_3CH_3$[29]	100
$Tl_2(MoO_3)_3PO_3CH_3$[30]	100
$Cs_2(WO_3)_3PO_3CH_3$[31]	100

[a] This work.

(67) Alvarez, S.; Avnir, D.; Llunell, M.; Pinsky, M. *New J. Chem.* **2002**, *26*, 996.
(68) Alvarez, S.; Alemany, P.; Casanova, D.; Cirera, J.; Llunell, M.; Avnir, D. *Coord. Chem. Rev.* **2005**, *249*, 1693.
(69) Alvarez, S.; Alemany, P.; Avnir, D. *Chem. Soc. Rev.* **2005**, *34*, 313.
(70) Salinas-Sanchez, A.; Garcia-Munoz, J. L.; Rodriguez-Carvajal, J.; Saez-Puche, R.; Martinez, J. L. *J. Solid-State Chem.* **1992**, *100*, 210.
(71) Preiser, C.; Losel, J.; Brown, I. D.; Kunz, M.; Skowron, A. *Acta Crystallogr., Sect. B: Struct. Sci.* **1999**, *B55*, 698.
(72) Brown, I. D. *The Chemical Bond in Inorganic Chemistry: The Bond Valence Model*, 1st ed.; Oxford University Press: Oxford, U.K., 2002.

powder SHG measurements have not been performed. Thus, we resynthesized the materials and measured the SHG efficiencies. As seen in Table 6, there is clearly a marked difference in the SHG efficiency between the Class 1 and Class 2 HTOs. For the Class 1 HTOs, the SHG efficiencies are between $30-50 \times \alpha\text{-}SiO_2$, whereas for the Class 2 HTOs, the SHG efficiencies range between $100-400 \times \alpha\text{-}SiO_2$. This SHG efficiency difference can be easily understood by examining the respective topologies. As we have discussed, with the Class 1 HTOs, the octahedral layers are capped on both sides by either lone-pair or methyl phosphonate groups. The "acentricity" associated with these groups effectively cancel, because they are directed in an antiparallel manner. Thus, the observed SHG efficiency is mainly attributable to the distortions that occur within the octahedral layers. In these layers, the V^{5+} cations are displaced toward an edge of their oxide octahedra. These local distortions only constructively add in part within the layer, i.e., some cancellation occurs. Thus, the resulting SHG efficiency for the Class 1 HTOs is reduced. The SHG efficiency observed in the Class 2 HTOs are, in some instances, more than an order of magnitude larger, compared to the Class 1 HTOs. The Class 2 HTOs have the lone-pair or methyl phosphonate group on one side of the octahedral layer. The "acentricity" associated with these groups are aligned and thus substantially contribute to the SHG efficiency. The transition-metal distortions within the layers are toward a face of their oxide octahedron, and similar to the Class 1 HTOs, there is partial constructive addition. Thus, the large SHG efficiencies with the Class 2 HTOs are mainly attributable to the alignment of the lone-pair or methyl phosphonate groups, but they are also augmented by the partial constructive addition of the transition-metal cation within the octahedral layers. It is also interesting to note that the Class 2 HTOs that do not contain a lone-pair group (e.g., $Cs_2(MoO_3)_3PO_3CH_3$, $Tl_2(MoO_3)_3PO_3CH_3$, and $Cs_2(WO_3)_3PO_3CH_3$) have SHG efficiencies that are substantially smaller, compared to Class 2 HTOs that contain a lone-pair group, e.g., $Cs_2(MoO_3)_3(TeO_3)$, $Tl_2(MoO_3)_3TeO_3$, and $Cs_2(WO_3)SeO_3$. This indicates, perhaps not too surprisingly, that the SHG efficiency contribution from a lone-pair polyhedron is greater than a methyl phosphonate group.

Acknowledgment. We thank the Robert A. Welch Foundation (Grant E-1457), the ACS PRF 47345-AC10, and the NSF (DMR-0652150) for support.

Supporting Information Available: This material is available free of charge via the Internet at http://pubs.acs.org.